Published in final edited form as:
J Am Coll Cardiol. 2011 June 21; 57(25): 2516–2526. doi:10.1016/j.jacc.2011.02.036.

Two-Dimensional Intravascular Near-Infrared Fluorescence Molecular Imaging of Inflammation in Atherosclerosis and Stent-Induced Vascular Injury

Farouc A. Jaffer, MD PhD FACC[*,1,2], **Marcella A. Calfon, MD PhD**[*,1], **Amir Rosenthal, PhD**[1,3], **Georgios Mallas, MSc**[1,4], **R. Nika Razansky, PhD**[3], **Adam Mauskapf, BS**[1], **Ralph Weissleder, MD PhD**[5], **Peter Libby, MD FACC**[6], and **Vasilis Ntziachristos, PhD**[3]

[1]Cardiovascular Research Center and Cardiology Division, Massachusetts General Hospital, Harvard Medical School, Boston, MA

[2]Center for Molecular Imaging Research, Massachusetts General Hospital, Harvard Medical School, Boston, MA

[3]Institute for Biological and Medical Imaging (IBMI), Helmholtz Center Munich & Technical University of Munich, Germany

[4]Department of Electrical and Computer Engineering, Northeastern University, Boston, MA

[5]Center for Systems Biology, Massachusetts General Hospital, Boston, MA

[6]Cardiovascular Division, Brigham and Women's Hospital, Harvard Medical School

Abstract

Objectives—To develop a two-dimensional intravascular near-infrared fluorescence (NIRF) imaging strategy for investigation of arterial inflammation in coronary-sized vessels.

Background—Molecular imaging of arterial inflammation could provide new insights into the pathogenesis of acute myocardial infarction stemming from coronary atheromata and implanted stents. Presently few high-resolution inflammation approaches can image inflammation in coronary-sized arteries in vivo.

Methods—A new 2.9F rotational, automated pullback two-dimensional imaging catheter was engineered and optimized for 360-degree viewing intravascular NIRF imaging. In conjunction with the cysteine protease-activatable imaging reporter Prosense VM110, intra-arterial 2D NIRF imaging was performed in rabbit aortas with atherosclerosis (n=10) or implanted coronary bare metal stents (n=10, 3.5mm diameter, day 7 post-implantation). Intravascular ultrasound (IVUS) provided co-registered anatomical images of arteries. After sacrifice, specimens underwent ex vivo NIRF imaging, fluorescence microscopy, and histological and immunohistochemical analyses.

Results—Imaging of coronary artery-scaled phantoms demonstrated 8-sector angular resolution and submillimeter axial resolution, nanomolar sensitivity to NIR fluorochromes, and modest NIRF light attenuation through blood. High-resolution NIRF images of vessel wall inflammation with signal-to-noise ratios > 10 were obtained in real-time through blood, without flushing or occlusion. In atherosclerosis, 2D NIRF, IVUS-NIRF fusion, microscopy, and immunoblotting

Correspondence: Farouc Jaffer and Vasilis Ntziachristos, F. Jaffer: MGH CVRC, Simches Research Building, Room 3206, 185 Cambridge St, Boston, MA 02114, Tel: 617-724-9353, fjaffer@mgh.harvard.edu, V. Ntziachristos: Institute for Biological and Medical Imaging (IBMI), Technische Universität München and Helmholtz Zentrum München, Ingolstaedter, Landstrasse 1, 85764 Neuherberg, Germany; v.ntziachristos@tum.de.
*Denotes equal author contribution

studies provided insight into the spatial distribution of plaque protease activity. In stent-implanted vessels, real-time imaging illuminated an edge-based pattern of stent-induced arterial inflammation.

Conclusions—A new 2D intravascular NIRF imaging strategy provides high-resolution in vivo spatial mapping of arterial inflammation in coronary-sized arteries, and reveals increased inflammation-regulated cysteine protease activity in atheromata and stentinduced arterial injury.

Keywords

intravascular imaging; inflammation; atherosclerosis; stent; molecular imaging

INTRODUCTION

Thrombotic complications of atherosclerosis and implanted coronary stents include myocardial infarction and sudden cardiac death. Accordingly there exists a compelling need to identify patients that harbor thrombosis-prone plaques and/or implanted stents, and also to monitor interventions aimed at their mitigation. At present however, clinicians lack the tools to gauge biological aspects of atheromata and stented arteries.

The biological characteristics of the arterial wall critically influence atherogenesis and plaque thrombosis (1,2), as well as the hyperplastic and thrombotic complications of arterial stenting (3,4). Molecular imaging strategies now afford an approach to reach beyond anatomy, and visualize in vivo atheroma inflammation, angiogenesis, apoptosis, oxidative stress, and calcification (5,6). Yet while clinically feasible for larger vessels such as the carotid and the aorta, high-resolution clinical molecular imaging strategies for the coronary arteries remain scarce, primarily due to the small imaging target volume, and multiple sources of image degradation, including cardiac and respiratory motion, and blood flow.

In vivo NIRF visualization approaches appear attractive for human coronary arterial molecular imaging (7). A recent preliminary study demonstrated 1D NIRF sensing (non-imaging) of atheroma inflammation in small diameter (1.5–2.0mm) vessels (8). This approach however did not enable two-dimensional imaging, nor sense NIRF signals in vessels of diameters more typical of human coronary arteries (2.5–3.5mm), nor evaluate inflammation due to coronary stent-induced injury. Additional limitations of the nonrotational 1D spectroscopic instrument included NIRF signal detection from only a small sector of the entire 360-degree arterial wall, limiting its sensitivity. In addition, the one-dimensional system lacked longitudinal (axial) anatomical accuracy due to manual pullback, and was subject to loss of distal vessel access due to required pullback of the sensing guidewire (as opposed to standard catheter-based imaging approaches).

To address these limitations and to advance the clinical potential of intracoronary NIRF molecular imaging, we present a new two-dimensional rotational and automated pullback NIRF intravascular catheter apparatus, capable of nanomolar-sensitive, intra-arterial molecular imaging in larger diameter coronary arteries. We utilize the 2D NIRF catheter to provide new biological insights into arterial inflammation in atheroma and coronary stent-induced vascular injury in vivo.

METHODS

Two-dimensional NIRF Imaging Device and Catheter

The apparatus (Figure 1, Supplemental Figure 1) houses a continuous-wave laser source operating at 750 nm (B&W Tek Inc, Newark, DE, USA) with electronically adjustable

output power. The catheter consists of an optical fiber (numerical aperture 0.37) within a polyethylene sheath (outer diameter 2.9F) that guides 750nm laser near-infrared light and collects the subsequent NIR fluorescence emission. The fiber is rotated and translated using mechanical stages to collect fluorescence and generate a 2D NIRF image. See Supplemental Methods.

Phantom Experiments

See Supplemental Methods.

Cysteine protease activity NIRF molecular imaging agent

To image cysteine protease activity, an activatable NIRF imaging agent (Prosense VM110 ("VM110"), 0.5 mg/kg, excitation/emission, 750nm/780 nm; VisEn Medical, Woburn, MA) was scaled up for use in atherosclerosis and arterial stent-injury in rabbits. This class of protease-activatable agents has been extensively validated and reports on cysteine protease activity, in particular cathepsin B (8–10).

Rabbit Atherosclerosis

Atherosclerotic lesions rich in inflammatory cells in New Zealand white rabbits were induced by balloon-injury and hypercholesterolemic diet as performed previously (8). Intravascular 2D NIRF imaging of atheroma inflammation (n=10 total; n=7 VM110, n=3 saline) was performed at 8 weeks after injury. An additional control group consisted of normal rabbits (n=2) injected with VM110 (0.5 mg/kg) twenty-four hours before imaging.

Stent-induced arterial injury

Bare metal coronary stents (3.5 mm diameter × 12 mm length) were implanted into the aorta of rabbits (n=10). Intravascular 2D NIRF imaging of stent-induced inflammation was performed at 7 days after injury, 24 hours after receiving Prosense VM110 (n=8, 0.5 mg/kg) or saline (n=2). See Supplemental Methods.

Intravascular NIRF and IVUS imaging

On the day of imaging, animals were anesthetized as described in the supplemental methods. A 5F introducer was inserted into the right carotid artery using fluoroscopic and angiographic guidance. Iodinated contrast was injected and baseline x-ray angiography was recorded using standard cineangiography. An IVUS catheter was inserted over an 0.014" guidewire and serial pullbacks were performed (Galaxy IVUS System, Boston Scientific/Scimed, Inc.) from the iliac bifurcation to the renal arteries, with a pullback length of 100 mm. Next, the monorail NIRF catheter was advanced over the guidewire. To cover the entire IVUS-imaged vessel and understand reproducibility of the NIRF signal profiles, the NIRF catheter was advanced into the iliac artery and 3–4 contiguous, 110 mm total length pullbacks were performed (rotational speed 30–100 rpm). Animals were then euthanized and the iliac and aorta were resected. The NIRF catheter was gently reintroduced into lumen of the aorta and ex vivo NIRF pullbacks were repeated up to 3 times. Corresponding images were aligned using iliac bifurcation and renal arteries as landmarks, and radiopaque catheter markers as fiducials. Areas of plaque and normal vessel were confirmed by IVUS images.

Fluorescence reflectance imaging (FRI)

Resected vessels underwent multiwavelength FRI (OV110; Olympus, Japan; equipped with an NIR filter set (Omega Optical, Brattleboro, VT): bandpass excitation 716–756 nm, bandpass emission 780–820 nm). Multiple exposure times (0.1–60sec) for each wavelength and acquired images were exported as DICOM files for further analyses. Due to vessel shrinkage after resection, the aorta and the iliac vessels were manually elongated to in vivo

measured lengths. ROIs were traced manually after visual identification of normal vessel, background, plaque, and stented zones (Osirix version 2.7.5, A. Rosset). Stent ROIs included 3 mm of tissue at proximal and distal edge respectively (total length of ROI drawn was 18 mm for 12 mm stent). Target-to-background ratios (TBRs) were calculated for each region of interest by dividing the mean ROI signal of target by adjacent vessel background (normal vessel). For SNR calculations, the mean ROI signal of target was divided by the standard deviation of background signal for each image.

Fluorescence Microscopy

Fluorescence microscopy of plaque and normal vessel sections was performed on adjacent sections from fresh-frozen rabbit arteries and the images were captured and processed using an epifluorescence microscope (Eclipse 80i, Nikon Instruments, Melville, NY) with filter sets for NIRF (excitation, 673-48 nm; dichroic mirror, DM750; emission, 765–835 nm; exposure time, 30 seconds) and autofluorescence (excitation, 460–500 nm; dichroic mirror, DM505; emission, 510–560 nm; exposure time, 1 second).

Statistical Analyses

In vivo SNR and TBR values were reported as median and quartiles [25^{th} percentile, 75^{th} percentile] (Prism 5.0c, GraphPad, La Jolla CA). Statistically significant differences between two groups were determined using the Mann-Whitney U test for unpaired observations, and the Wilcoxon matched-pairs signed-ranks test for paired observations. Among multiple groups, significance was assessed via the Kruskal-Wallis test. A p-value of $p<0.05$ was considered statistically significant.

See Supplemental Methods for in vivo atherosclerosis and stent NIRF SNR and TBR measurements, NIRF-IVUS image fusion, histopathology, and immunoblotting.

RESULTS

In vitro evaluation of a nanomole-sensitive rotational, automated pullback catheter platform for intravascular NIRF molecular imaging

In vitro performance (image generation, sensitivity, axial resolution, angular resolution) of the 2D NIRF system was tested in custom-built coronary-scale phantoms (Supplemental Figure 2). SNR measurements were first obtained for various fluorochrome concentrations immersed in saline and blood-like solution, respectively (Figures 2A–B). In saline, a 100 nM fluorochrome concentration was detected at fiber-to-target distances of up to 4.5 mm. In blood-like solution, the detected NIRF signal decayed exponentially with distance ($d_{1/2}$ = 0.33 mm). The 50 μM and 100 nM NIRF phantoms were detected at fiber-to-target distances of 2.5 mm and 1.2 mm, respectively. The overall system sensitivity improved by an order-of-magnitude compared to an earlier 2D prototype (11).

In saline, the angular resolution, or the ability to discern discrete sectors along the circumference of the vessel, ranged from 24° to 29°, and was relatively unaffected by distance (Figure 2C). The angular resolution was lower in blood-like solution (35° to 42°) due to light scattering, but still demonstrated the ability to resolve > 8 sectors at a fiber-to-target distance of 3.0mm. The axial resolution, or ability to resolve fluorescence signals along the long axis of the vessel, varied as a function of the fiber-to-target distance (Figure 2D). In blood the resolution depended non-linearly on the fiber-to-target distance, reaching 1.0 mm resolution at a 2.0 mm fiber-to-target distance.

Intravascular NIRF high-resolution imaging of protease activity in rabbit atheromata in blood-filled arteries

The validated 2D NIRF catheter was then used to generate 2D geometrically accurate maps of inflammation in atherosclerosis. Twenty-four hours after injection of Prosense VM110 (n=7) or saline (n=3), atheroma-bearing rabbits (n=10) underwent multimodality x-ray angiography, IVUS, and in vivo NIRF imaging. In atherosclerotic animals injected with VM110, in vivo NIRF catheter imaging revealed intense focal signals along pullbacks, indicating elevated cysteine protease activity (Figure 3A). Ex vivo FRI confirmed high NIRF signals within plaques (Figure 3B–3C). In contrast, both saline-injected atherosclerotic and normal, VM110-injected animals demonstrated reduced NIRF signals on in vivo and ex vivo NIRF imaging (Figures 3D–3I). The ex vivo vessel SNR was significantly greater in VM110-injected atheroma-bearing rabbits than control atheroma/saline rabbits and control normal/VM110 rabbits (229.1 [154.3, 311.6] vs. 90.2 [76.3, 90.5] and 83.6 [70.9, 96.2], p=0.01, Figure 4A). In the two atherosclerosis groups (Figure 4B–4C), the ex vivo plaque SNR and TBR were > 140% higher in the VM110 group compared to the saline group (plaque SNR 218.5 [194.3, 348.0] vs. 90.5 [77.9, 90.9], p=0.01; plaque TBR 2.4 [2.0, 3.3] vs. 1.0 [1.0, 1.1], p=0.01).

Radiopaque markers and vascular fiducials allowed reliable co-registration of intravascular NIRF and IVUS images, and demonstrated NIRF signal in areas of IVUS-demarcated atherosclerosis (Figure 5). Focality of NIRF signal enhancement was appreciable in both the angular and axial dimensions (Figure 5D–5E), consistent with the eccentric, multi-focal profile of IVUS-verified atherosclerosis. Areas of normal appearing vessel (lack of plaque detected by IVUS) demonstrated little NIRF background signal. The Prosense VM110 group showed significantly higher vessel SNR in vivo, with a greater than 170% increase over to the other two control groups (p=0.04, Figure 6A). In rabbits with atheromata, the in vivo plaque SNR and TBR was > 450% higher in the VM110 compared to the saline group (SNR 12.6 [8.1, 20.6] vs. 1.3 [0.9, 2.1], p=0.02; TBR 6.3 [4.3, 9.4] vs. 1.1 [0.9, 1.4], p=0.02; Figure 6B–6C). In addition, augmented NIRF proteinase signal also appeared in an area of injury-induced arterial dissection adjacent to atheroma (Supplemental Figure 3).

Elevated in vivo and ex vivo plaque NIRF signal associates with the cysteine protease cathepsin B

Advanced plaques and early plaques (Figure 7A–7B) demonstrated strong cathepsin B immunoreactivity within the intima and media, consistent with augmented proteinase expression (precursor and mature form) within macrophages and smooth muscle cells (12,13). Intimal cathepsin B staining colocalized with immunohistochemical detection of RAM-11 positive intimal macrophages. In contrast, the normal vessel wall produced minimal cathepsin B and macrophage staining (Figure 7C).

Fluorescence microscopy revealed focal NIR fluorescence in the intima of advanced plaques (Figure 7A). Early atheromata with cathepsin B enzyme presence (Figure 7B) did not emit NIR fluorescence, suggesting lower cysteine protease activity in early-stage plaques. Fluorescence microscopy further revealed that the NIRF signal was plaque-specific and VM110-specific, as autofluorescence signal (535nm fluorescence) colocalized with elastin-rich medial fiber signals. Slight medial autofluorescence was visualized in the 800nm channel, and as expected was substantially lower than autofluorescence at 535nm (14,15). Immunoblotting of normal and plaque-rich aorta showed increased expression of both precursor and mature cathepsin B protein in plaque-rich vessels (Figure 7D).

Intravascular NIRF molecular imaging of coronary stent-induced arterial inflammation reveals a stent edge-based injury pattern in vivo

Extended arterial inflammation characterizes unhealed coronary stents that may provoke stent thrombosis (3,4). To investigate and image arterial wall inflammation in vivo following stent deployment, New Zealand white rabbits underwent aortic balloon injury (n=10) followed by deployment of a bare metal coronary stent (3.5×12mm). Six days following stent implantation, rabbits received intravenous Prosense VM110 (n=8) or saline (n=2). The next day (day 7) rabbits underwent in vivo multimodality x-ray angiography, IVUS and intravascular NIRF imaging. In stent-injured vessels, increased in vivo NIRF signal localized at the edges of the implanted stents, and particularly at the leading or distal stent edge (Figure 8), suggesting that stent-based injury occurred at sharp transition points. In addition, as augmented protease signal was noted 1–2 mm away from the stent edge, another mechanism of vessel wall inflammation could be due to balloon extension ("overhang") injury at the proximal and distal stent edges. Intriguingly, very high magnification ex vivo FRI of the resected coronary stents revealed increased cysteine protease activity at the greater curvature of stent struts (Figures 9C–9E).

The maximal SNR recorded during pullbacks occurred at stent edges and was significantly greater than uninjured vessel segments for both in vivo NIRF pullbacks (23.1 [11.7, 27.0] vs. 1.1 [1.0, 3.7], p=0.02) and ex vivo FRI (234.5 [160.6, 274.2] vs. 110.7 [100.7, 135.0], p=0.008), Figures 9F–9G). The maximum stent TBR was 18.3 [2.8, 25.7] in the VM110 group vs. 1.2 [1.0, 1.4] in the saline group, p=0.056) for the in vivo NIRF pullbacks. Immunoblot analyses also revealed augmented cathepsin B proteases in extracts of injured vessel wall encasing implanted coronary stents (Figure 9H).

DISCUSSION

Complications of atherosclerosis and improperly healed coronary stents include acute myocardial infarction and sudden cardiac death. To address the unmet clinical need for high-resolution molecular imaging strategies targeted to coronary-sized arteries, we engineered and validated an intravascular catheter-based two-dimensional NIRF imaging platform. The intravascular molecular imaging results demonstrate spatial mapping of arterial inflammation (as mediated by VM110 activation and fluorescence generation following cleavage by cysteine proteases) in atherosclerosis, as well as in coronary-stent induced vascular injury and arterial dissection. Anatomically accurate images were obtained in real-time, through blood, and without the need for flushing or occlusion.

The optimized 2D NIRF imaging system demonstrated several advantages in vivo compared to a prior guidewire device (8) and a recent less sensitive 2D prototype (11) that did not support in vivo molecular imaging. These advantages include: (i) the ability to obtain two-dimensional molecular images of multi-focal vascular inflammation with 360-degree coverage and accurate geometry; (ii) the ability to image vascular inflammation in blood-filled arteries of 3.5mm diameter, significantly larger than demonstrated previously (1.5–2.0mm)(8), thereby offering greater applicability to vessels of the caliber of human coronary arteries; (iii) co-registration of high-resolution IVUS that enabled fusion molecular-anatomical imaging; and (iv) implementation of a clinical-type 2.9 Fr monorail catheter that avoids loss of distal vessel guidewire access.

Intravascular NIRF can image biological processes of importance in atherosclerosis and stent healing including inflammation, angiogenesis, fibrin deposition, and remodeling (16). In atherosclerosis, inflammation is a key biological process that promotes atherogenesis and plaque rupture, and characterizes high-risk, vulnerable plaques (1). In particular, proteinases participate as key mediators of inflammation, facilitating matrix degradation, remodeling,

leukocyte recruitment, and elastic lamina breakdown. In conjunction with the NIRF molecular imaging agent Prosense VM110, the intravascular NIRF catheter enabled high-resolution imaging of cysteine proteinase activity in atheromata, stent injury, and intimal dissection induced by arterial intervention. Subsequent histological and biochemical analyses linked the NIRF signal to cysteine proteases, a marker of inflamed plaques. In addition, fluorescence microscopy revealed differences between NIRF imaging of enzyme activity and immunohistochemical detection of enzyme presence (Figure 7). In contradistinction to the more extensive immunoreactive cathepsin B protein in the intima and media of early and advanced atheroma, NIRF-detected cysteine protease activity was restricted to the diseased intima of more established atheromata. Unlike IVUS and other structural imaging methods, NIRF imaging of atheroma assesses the activity of cathepsin B and related enzymes, and hence provides insight into the in vivo biology of inflamed plaques.

Stent thrombosis, a clinical syndrome that often causes acute myocardial infarction and cardiac death, may occur from incompletely healed coronary stents, typically characterized by impaired endothelialization, inflammation and fibrin deposition (3,4). At present, few approaches can visualize biological aspects of coronary-stent induced injury in vivo. The employed two-dimensional NIRF strategy provided new insights into in vivo arterial inflammation following implantation of bare metal coronary stents in rabbit aortas (Figure 8). The stent edges showed higher proteinase activity signal, and high-magnification ex vivo FRI demonstrated proteinase activity largely on the outer (greater) curvature of the employed bare metal stent. This effect may result from differential flow-mediated inflammation related to the configuration of the stent strut (17). The observed edge-based inflammatory injury patterns in vivo further support that stent geometry, design, and materials influence the risk of stent thrombosis and restenosis (18). Further studies may shed light on the differences in the temporal-spatial patterns of arterial inflammation surrounding implanted drug-eluting stents compared to implanted bare-metal stents.

A limitation to the current intravascular NIRF approach is surface-weighting of the NIRF signal as a function of fiber-to-wall distance, particularly in light-attenuating blood. This aspect limits the depth resolution of the NIRF signal, as well as optimal signal quantification for non-centered catheters. Possible compensation methods include the use of a focused fiber to image a more selective tissue volume, as well as mapping the luminal position of the NIRF catheter from co-registered IVUS information, as a first approximation, to correct the NIRF signal based on the fiber-to-wall distance. Of note is that plaque tissue is less likely to attenuate NIRF signals, based on prior tissue phantom studies (8). Additional sensitivity gains are anticipated with the use of focused and larger numerical aperture fibers to deliver and collect light more efficiently. Finally to enable accurate angular NIRF and IVUS co-registration, a limitation of the two separate NIRF and IVUS catheters, additional strategies employing 3D radiopaque fiducials may be helpful.

From a translational standpoint, intracoronary NIRF molecular imaging via optical catheters appears clinically viable, based on FDA approval of other light-based catheter approaches including optical coherence tomography/optical frequency domain imaging (19) and near-infrared spectroscopic chemical imaging (20) utilizing similar laser powers and catheter sizes. In addition, clinical approval of NIRF imaging agents appear promising based on the favorable safety profile of indocyanine green (21), a clinical NIR fluorochrome widely utilized in retinal angiography and historically in cardiac output studies. Clinical use of such novel imaging technologies will naturally first require safety studies of new NIRF imaging agents and intravascular catheters.

Ultimately, high-resolution molecular imaging of coronary arteries could provide a new approach to (i) investigate the natural history of inflammation in a variety of coronary arterial pathologies, including atherosclerosis, stent-induced vascular injury, dissection, arteritis and allograft vasculopathy; (ii) investigate novel pharmacotherapies designed to attenuate inflammation in coronary atherosclerosis; and (iii) to provide an in vivo biological framework to identify subjects with high-risk plaques and high-risk coronary stents predisposed to thrombosis.

Supplementary Material

Refer to Web version on PubMed Central for supplementary material.

Acknowledgments

We thank Claudio Vinegoni PhD, Guillermo Tearney MD PhD, Dana Brooks PhD, and Elazer Edelman MD PhD for helpful discussions, Yoshi Iwamoto BS for histopathological assistance, J. Luis Guerrero BS for assistance in surgical studies, Peter Waterman BS for assistance with FRI studies, and Robert W Yeh, MD MSc for statistical assistance.

Funding Sources: NIH R01 HL 108229 (F.A.J.), NIH R01 HL 80472 (P.L.), American Heart Association Scientist Development Grant #0830352N (F.A.J.), Howard Hughes Medical Institute Career Development Award (F.A.J.), Broadview Ventures (F.A.J, V.N.) Donald W. Reynolds Foundation (F.A.J., R.W., P.L.), and European Community's Seventh Framework Programme (FP7/2007-2013 under grant agreement n° 235689 to A.R.), and MGH William Schreyer Fellowship (M.A.C.).

ABBREVIATIONS

1D/2D	One/two dimensional
Fr	French
FRI	fluorescence reflectance imaging
HCD	high-cholesterol diet
NIRF	near-infrared fluorescence
ROI	region-of-interest
SNR	signal-to-noise ratio
TBR	target-to-background ratio

REFERENCES

1. Libby P. Inflammation in atherosclerosis. Nature. 2002; 420:868–874. [PubMed: 12490960]
2. Rader DJ, Daugherty A. Translating molecular discoveries into new therapies for atherosclerosis. Nature. 2008; 451:904–913. [PubMed: 18288179]
3. Luscher TF, Steffel J, Eberli FR, et al. Drug-eluting stent and coronary thrombosis: biological mechanisms and clinical implications. Circulation. 2007; 115:1051–1058. [PubMed: 17325255]
4. Nakazawa G, Finn AV, Joner M, et al. Delayed arterial healing and increased late stent thrombosis at culprit sites after drug-eluting stent placement for acute myocardial infarction patients: an autopsy study. Circulation. 2008; 118:1138–1145. [PubMed: 18725485]
5. Jaffer FA, Libby P, Weissleder R. Molecular imaging of cardiovascular disease. Circulation. 2007; 116:1052–1061. [PubMed: 17724271]
6. Sanz J, Fayad ZA. Imaging of atherosclerotic cardiovascular disease. Nature. 2008; 451:953–957. [PubMed: 18288186]

7. Calfon MA, Vinegoni C, Ntziachristos V, Jaffer FA. Intravascular near-infrared fluorescence molecular imaging of atherosclerosis: toward coronary arterial visualization of biologically high-risk plaques. Journal of Biomedical Optics. 2010; 15:011107–011106. [PubMed: 20210433]
8. Jaffer FA, Vinegoni C, John MC, et al. Real-Time Catheter Molecular Sensing of Inflammation in Proteolytically Active Atherosclerosis. Circulation. 2008; 118:1802–1809. [PubMed: 18852366]
9. Weissleder R, Tung CH, Mahmood U, Bogdanov A Jr. In vivo imaging of tumors with protease-activated near-infrared fluorescent probes. Nat Biotechnol. 1999; 17:375–378. [PubMed: 10207887]
10. Chen J, Tung CH, Mahmood U, et al. In vivo imaging of proteolytic activity in atherosclerosis. Circulation. 2002; 105:2766–2771. [PubMed: 12057992]
11. Razansky RN, Rosenthal A, Mallas G, Razansky D, Jaffer FA, Ntziachristos V. Near-infrared fluorescence catheter system for two-dimensional intravascular imaging in vivo. Opt Express. 2010; 18:11372–11381. [PubMed: 20588998]
12. Liu J, Sukhova GK, Sun J-S, Xu W-H, Libby P, Shi G-P. Lysosomal Cysteine Proteases in Atherosclerosis. Arterioscler Thromb Vasc Biol. 2004; 24:1359–1366. [PubMed: 15178558]
13. Lutgens SPM, Cleutjens KBJM, Daemen MJAP, Heeneman S. Cathepsin cysteine proteases in cardiovascular disease. FASEB J. 2007; 21:3029–3041. [PubMed: 17522380]
14. Vinegoni C, Razansky D, Hilderbrand SA, Shao F, Ntziachristos V, Weissleder R. Transillumination fluorescence imaging in mice using biocompatible upconverting nanoparticles. Opt Lett. 2009; 34:2566–2568. [PubMed: 19724491]
15. Vinegoni C, Razansky D, Figueiredo JL, Nahrendorf M, Ntziachristos V, Weissleder R. Normalized Born ratio for fluorescence optical projection tomography. Opt Lett. 2009; 34:319–321. [PubMed: 19183644]
16. Kim JW, Jaffer FA. Emerging Molecular Targets for Intravascular Imaging of High-Risk Plaques. Current Cardiovascular Imaging Reports. 2010; 3:237–247.
17. Moore JE Jr. Biomechanical issues in endovascular device design. J Endovasc Ther. 2009; 16 Suppl 1:I1–I11. [PubMed: 19317580]
18. Rogers C, Edelman ER. Endovascular stent design dictates experimental restenosis and thrombosis. Circulation. 1995; 91:2995–3001. [PubMed: 7796511]
19. Tearney GJ, Waxman S, Shishkov M, et al. Three-dimensional coronary artery microscopy by intracoronary optical frequency domain imaging. JACC Cardiovasc Imaging. 2008; 1:752–761. [PubMed: 19356512]
20. Waxman S, Dixon SR, L' Allier P, et al. In vivo validation of a catheter-based near-infrared spectroscopy system for detection of lipid core coronary plaques: initial results of the SPECTACL study. JACC Cardiovasc Imaging. 2009; 2:858–868. [PubMed: 19608137]
21. Hope-Ross M, Yannuzzi LA, Gragoudas ES, et al. Adverse reactions due to indocyanine green. Ophthalmology. 1994; 101:529–533. [PubMed: 8127574]

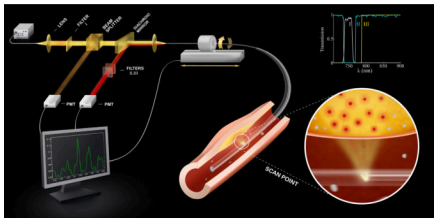

Figure 1.
Schematic of the constructed 2D NIRF imaging system. The tip of the fiber contains a right angle prism that reflects the guides laser light into the artery wall, and couples the subsequent fluorescent light back into the fiber. The fluorescent light is then directed to a dichroic beam-splitter that selectively reflects it into a photomultiplier tube. The beam passes additional filters to minimize the parasitic signals of laser photons and auto-fluorescence. The inset shows the spectra of the three filters (I,II,III) used in the system.

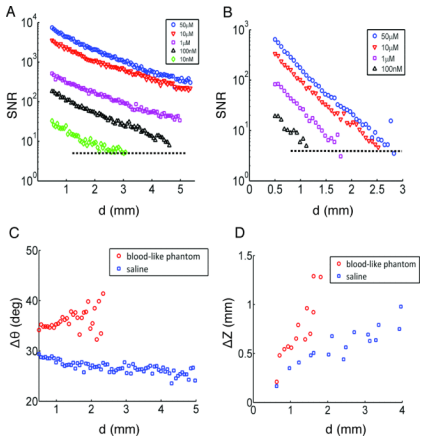

Figure 2.

Evaluation of the 2D NIRF apparatus in coronary artery scale phantoms. The SNR of the catheter for different fluorochrome concentrations measured in **(A)** saline and **(B**) blood-like solutions. **(C)** Angular and **(D)** axial resolution of the system in saline and blood-like solutions. The dashed line in A and B designates the sensitivity limit of the system, corresponding to SNR=4. d, distance from catheter-to-target; the fiber-to-target distance equals d+0.5mm.

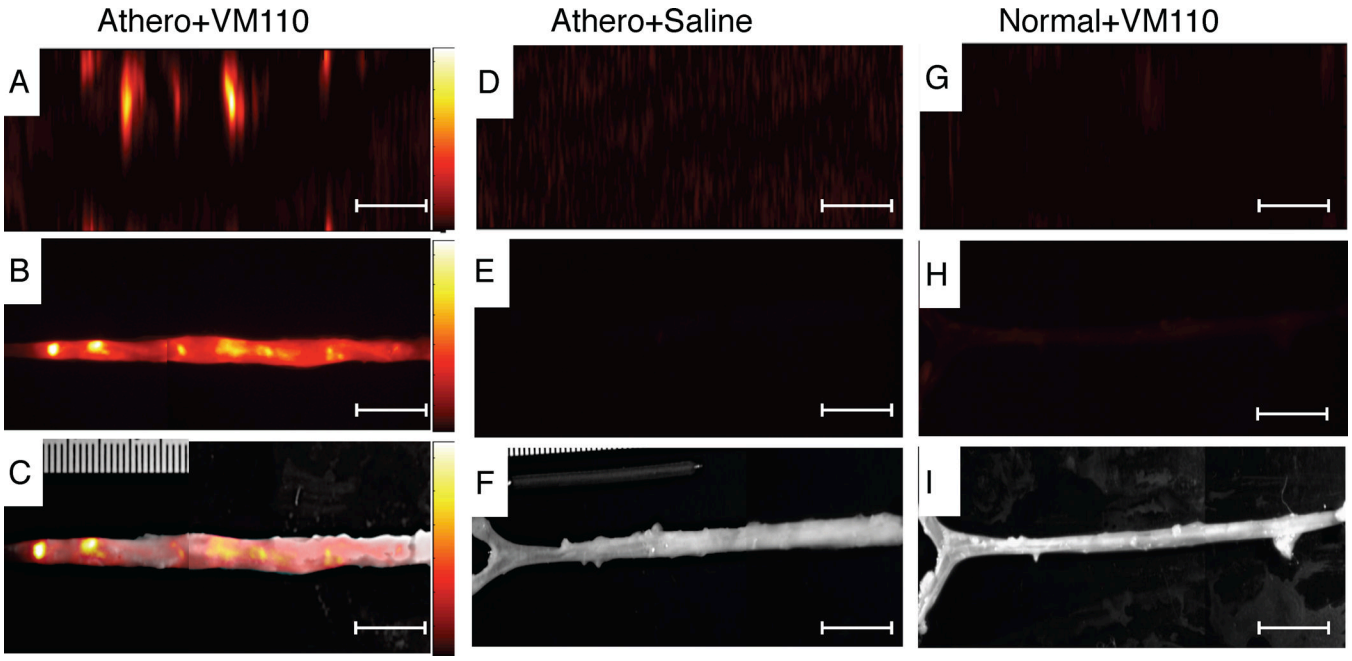

Figure 3.

In vivo high-resolution NIRF molecular imaging of cysteine proteinase activity in atherosclerosis. **(A)** Aorta from atherosclerotic rabbits injected with Prosense VM110 one day prior, and imaged in vivo with the intravascular NIRF catheter. **(B)** Ex vivo FRI at 800 nm and **(C)** ex vivo NIRF-white light fusion image. **(D)** Aortas from atherosclerotic rabbits injected with saline and imaged in vivo with the NIRF catheter, and (**E**) ex vivo FRI at 800nm and **(F)** ex vivo NIRF-white light fusion image. **(G)** Normal rabbit injected with VM110 and imaged with the intravascular NIRF catheter. **(H)** Ex vivo FRI at 800nm (1 sec) and **(I)** ex vivo NIRF-white light fusion image. In vivo and ex vivo fluorescence images were equally windowed and processed (color lookup table applies to all figures in each row). Scale bar, 10 mm.

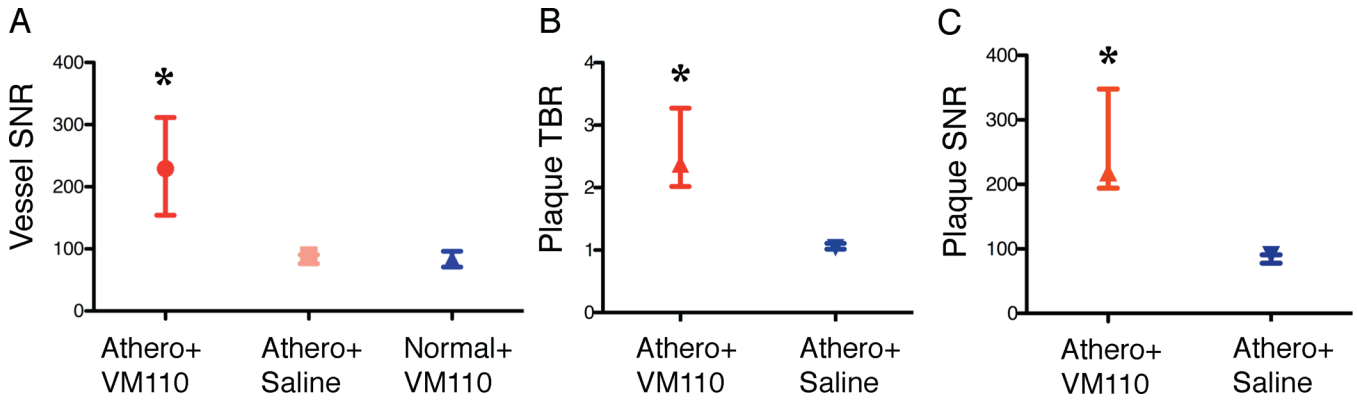

Figure 4.

Ex vivo NIR fluorescence reflectance imaging analyses of atheroma inflammation. The three experimental groups tested were: atherosclerosis+Prosense VM110 (Athero/VM110), atherosclerosis+saline (Athero+saline), and normal+Prosense VM110 (Normal/VM110), where Prosense VM110 is a protease-activatable NIRF imaging agent. **(A**) Ex vivo vessel SNR, (**B**) plaque TBR, and (**C**) plaque SNR from the three experimental groups. Athero=atherosclerosis. *p<0.05.

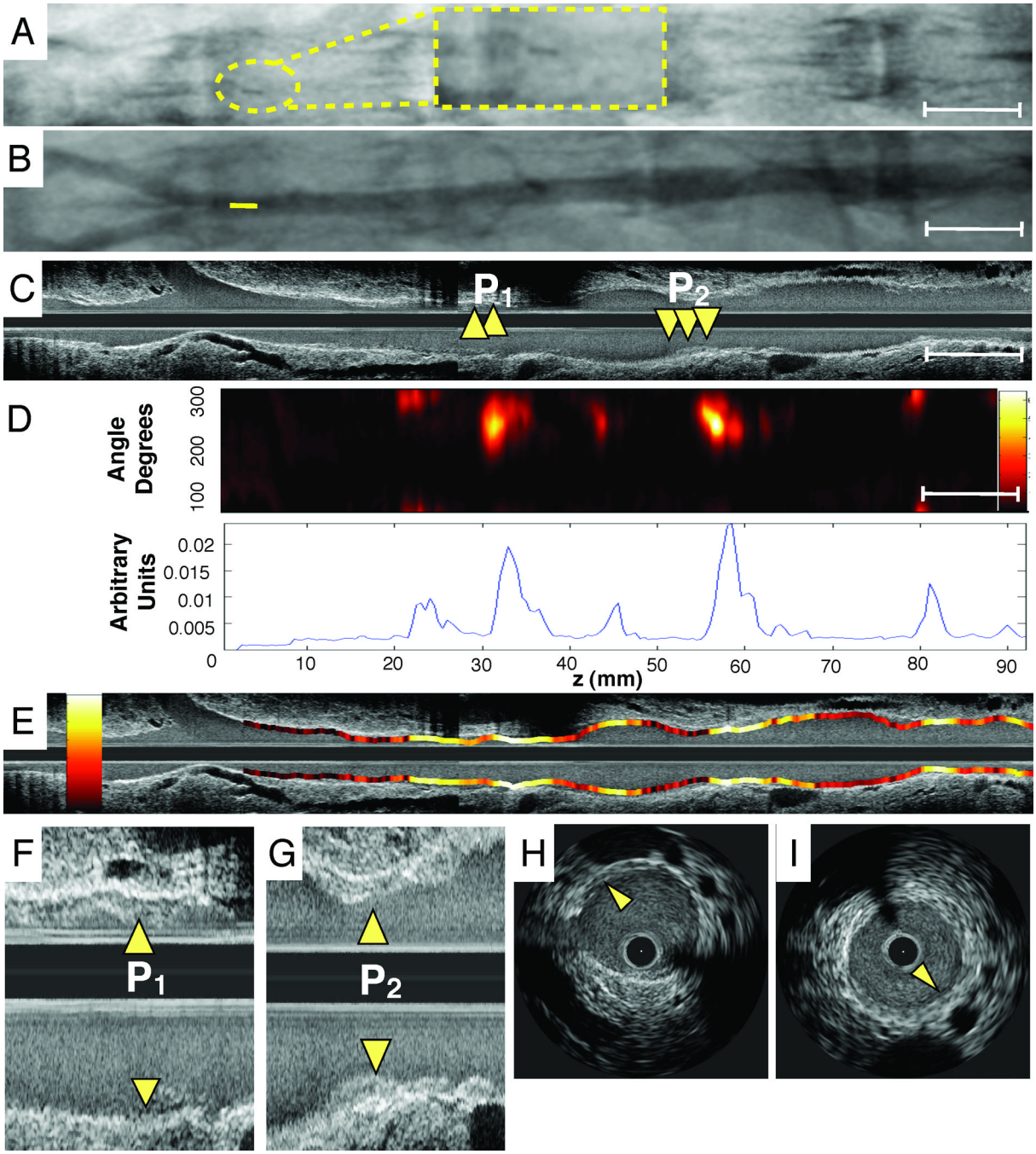

Figure 5.

Representative in vivo molecular and anatomical imaging of inflamed atheromata. **(A)** Angiographic appearance (with inset high magnification image in dotted yellow lines) of radiopaque tip of NIRF catheter positioned just proximal to the iliac bifurcation, enabling co-registration with IVUS. **(B)** Angiogram of the atherosclerotic iliac and aorta. Tip of the NIRF catheter at pullback initiation confirming its intravascular position (colored yellow). **(C)** Longitudinal IVUS image of the abdominal aortoiliac arteries. Arrows demarcate IVUS-detectable mildly stenotic plaques (P_1,P_2). **(D)** Image of NIRF catheter pullback aligned with the angiogram and IVUS image demonstrates NIRF signal in small volume plaques, in >3.0 mm diameter arteries. Corresponding 1D plot of the angle-averaged 2D NIRF intensity

pullback below. **(E)** Longitudinal superimposed NIRF and IVUS fusion images (yellow/white=strongest NIRF signal intensity, red/black=lowest NIRF signal intensity). **(F,G)** High magnification image of plaque zones P_1 and P_2. Arrows indicate minimally stenotic atherosclerotic plaques. **(H, I)** Axial IVUS images from zone P_1 and P_2.

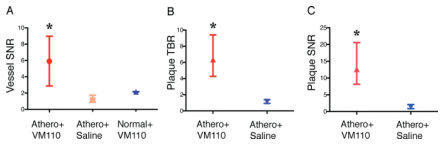

Figure 6.

NIRF signal analyses of atheroma inflammation detected in vivo by the 2D NIRF catheter. **(A,B,C)** In vivo plaque TBR, SNR and vessel SNRs from atherosclerotic animals injected with either Prosense VM110 (Athero+VM110) or saline (Athero+saline), or from normal (non-atherosclerotic) animals injected with Prosense VM110 (normal+VM110). *$p<0.05$.

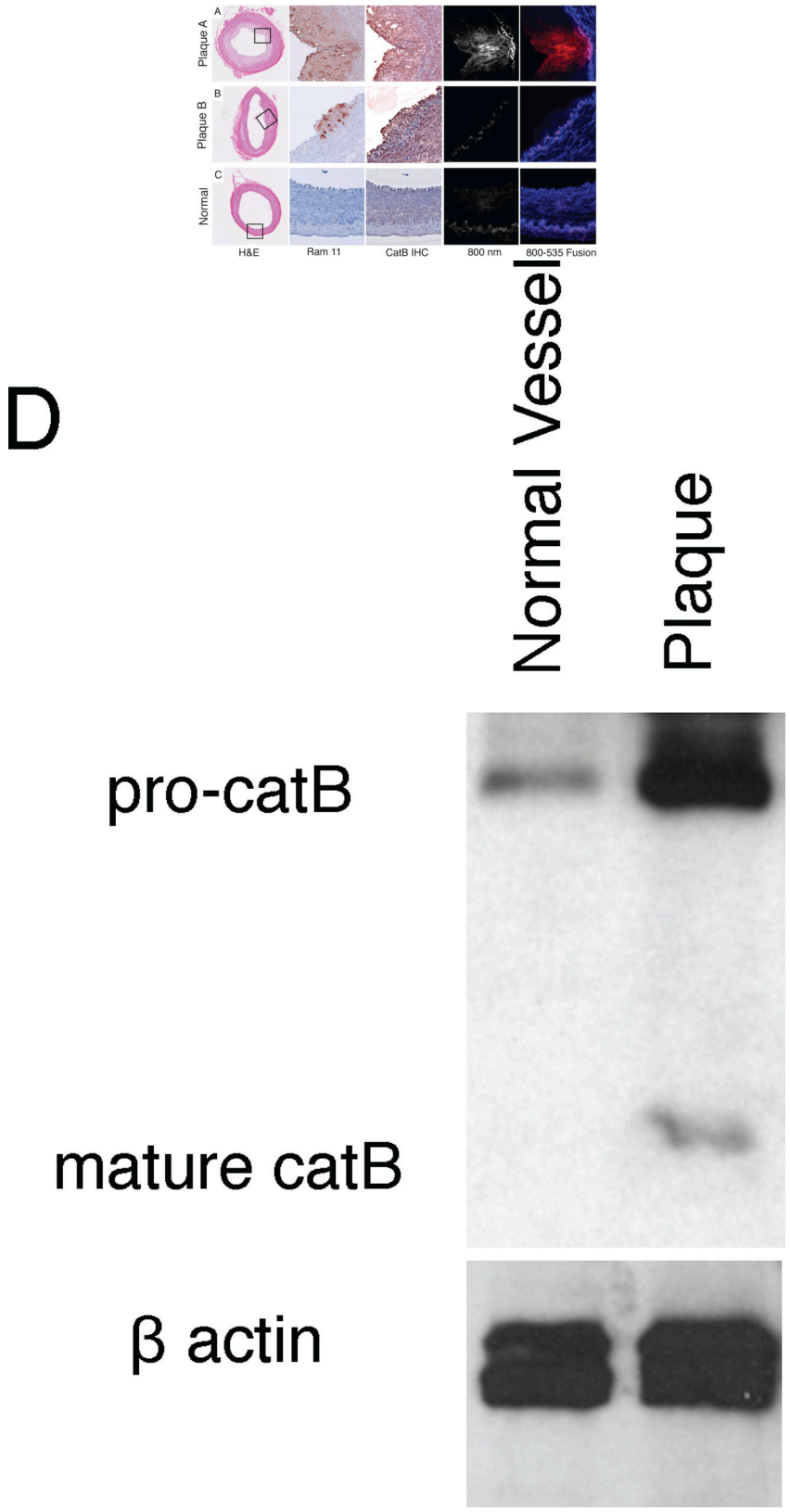

Figure 7.

Histopathological and immunoblotting assessments of aortic inflammation. In each row, the five images depict correlative arterial sections of hematoxylin and eosin staining (10X), immunoreactive macrophages (RAM-11, 20X), immunoreactive cathepsin B (catB, 20X), NIR fluorescence at 800nm, and merged 800nm-535 nm fluorescence, with red color denoting 800nm signal induced by cysteine protease activation of Prosense VM110, and blue color denoting signal at 535nm originating from autofluorescence. (**A**) In an advanced plaque, immunoreactive macrophages and cathepsin B, and intimal NIRF protease activity signals are evident. **(B)** Early stage atheroma demonstrates macrophages and cathepsin B in the intima and media but little NIRF cysteine protease activity (800nm image). **(C)** Section of a normal artery. Elastin fibers provide a source of autofluorescence (blue color) on fusion fluorescence microscopy images. (**D**) Cathepsin B and β-actin immunoblot of lysates from normal and plaque containing vessel demonstrates cathepsin B in atherosclerotic aortas. Pro-catB denotes the 46 kD pre-cathepsin B band, and mature catB denotes the 25 kD and 30 kD cathepsin B bands.

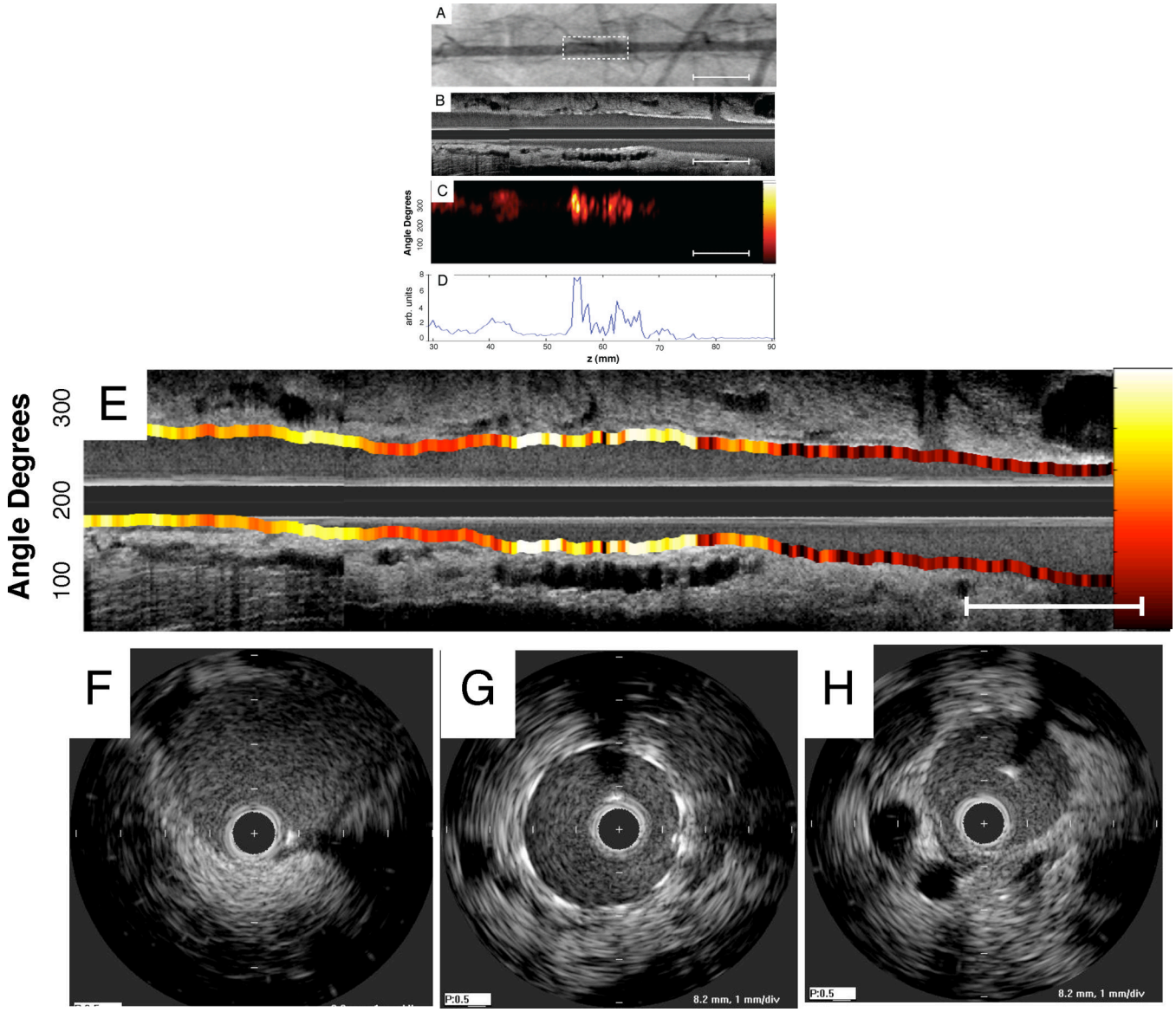

Figure 8.

Representative multimodality NIRF molecular and IVUS anatomical imaging of arterial inflammation at day 7 following coronary stent implantation. **(A)** Angiogram of an implanted bare metal stent in the abdominal aorta. Dotted rectangle denotes stent position. **(B,C)** Longitudinal IVUS and NIRF catheter pullbacks demonstrate NIRF signal within the stent. NIRF signal collection was performed through blood without flushing, in 3.5mm diameter vessels. **(D)** Corresponding 1D plot of the angle-averaged 2D NIRF signal at each axial point. **(E)** Longitudinal IVUS and NIRF fusion image (yellow/white=strongest NIRF signal intensity, red/black=lowest NIRF signal intensity). **(F,G,H)** Axial IVUS images from PTCA alone, stent and normal vessel zones, respectively.

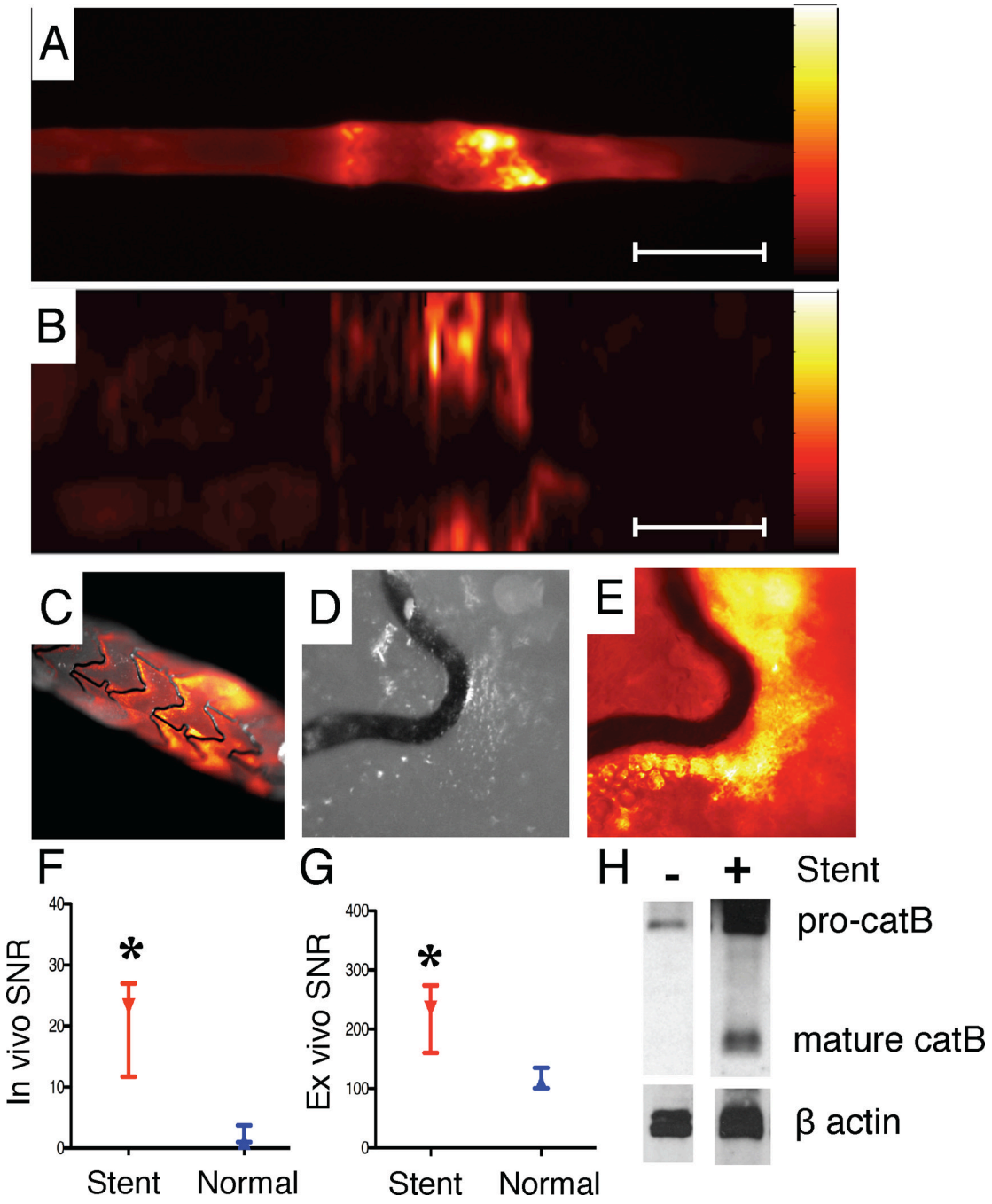

Figure 9.

NIRF imaging of stent injury. **(A)** Ex vivo FRI at 800nm reveals augmented NIRF protease activity at stent edges. **(B)** Corresponding ex vivo intravascular NIRF pullback also detected stent-based NIRF signal increases. **(C)** Ex vivo NIRF-white light fusion image of the stent, **(D)** high-magnification white light and **(E)** high-magnification NIRF image reveals signal along the greater curvature of stent struts. **(F)** In vivo and **(G)** ex vivo SNR in the normal and stented aorta (paired observations). **(H)** Immunoblot of cathepsin B (catB) staining in normal and stented rabbit aorta. Pro-catB denotes the 46 kD pre-cathepsin B band, and mature catB denotes the 25 kDa and 30 kDa cathepsin B bands. Scale bar, 10 mm. *$p<0.05$.